CRYSTAL GROWTH & DESIGN

pubs.acs.org/crystal

Article

Structural and Magnetic Studies of a Discrete Tetranuclear Complex Featuring an Oxalato-Bridged $Ni_3^{II}Cr^{III}$ Cluster

Published as part of Crystal Growth & Design special issue "Frontiers of Molecular Magnetism".

Shubham Bisht, Shuanglong Liu, Kavipriya Thangavel, Dibya Jyoti Mondal, Xinsong Lin, Sandugash Yergeshbayeva, Stephen Hill,* Hai-Ping Cheng,* and Michael Shatruk*

Cite This: *Cryst. Growth Des.* 2025, 25, 5834−5844

Read Online

ACCESS | Metrics & More | Article Recommendations | Supporting Information

ABSTRACT: A tetranuclear oxalate-bridged complex was synthesized by a reaction between the tris(oxalato)chromium(III), $[Cr(C_2O_4)_3]^{3-}$, and a 3-fold excess of the Ni^{2+} ion capped with a tetradentate 1,4,7,10-tetraazacyclododecane (cyclen) ligand. The structure of $[Ni_3(cyclen)_3Cr(\mu\text{-}C_2O_4)_3](ClO_4)_3$ (**1**), established by X-ray diffraction, features a triangle of the Ni^{2+} ions centered by the $[Cr(C_2O_4)_3]^{3-}$ anion through bridging oxalate ligands. The Ni^{2+} and Cr^{3+} ions exhibit oxalate-mediated ferromagnetic exchange coupling, which leads to the $S = 9/2$ ground state. Both simulation of the magnetic data and theoretical calculations show that the exchange coupling is isotropic. Although the study of a model mononuclear complex $[Ni(cyclen)(MeCN)_2]^{2+}$ by high-field EPR spectroscopy reveals a substantial zero-field splitting on the Ni^{2+} ion, complex **1** exhibits weak magnetic anisotropy within a giant spin model. This difference is attributed to dilution of the single-ion anisotropies of the Ni^{2+} ions due to their nearly symmetrical (trigonal) arrangement around the central Cr^{3+} ion. CASSCF calculations provided reasonable zero-field splitting parameters and Landé *g*-factors for the Ni^{2+} and Cr^{3+} ions in complex **1**.

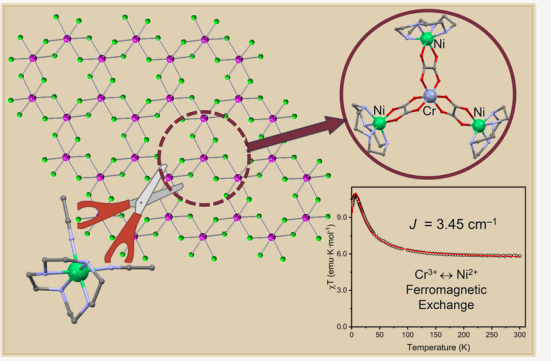

INTRODUCTION

Multinuclear complexes of transition and rare-earth metals have proven to be a boundless source of knowledge and discovery in the area of molecular magnetism,[1−5] especially as finite-size mimics that enable deeper fundamental insights into properties of extended-structure materials, e.g., solid-state oxides and intermetallics. Moreover, studies of such complexes led to the discovery of magnetic phenomena that mirror, on the macroscale, ferroic orders observed in extended solids, yet show unique features that emerge only at the molecular (quantum) level. The prominent examples are single-molecule magnets (SMMs)[4,6−11] and less-common single-molecule toroics (SMTs),[12−14] analogues of ferromagnets and ferrotoroidics, respectively. These studies also spurred a variety of innovative and creative synthetic strategies to bring the metal ions into close proximity by means of bridging ligands and optimize the resulting magnetic energy states and anisotropies, while limiting such an assembly to compact molecular units (clusters) to avoid the loss of distinct single-molecule properties. In this context, the synthesis of heterometallic complexes with controlled magnetic exchange interactions between metal ions remains an extensively researched and challenging area of coordination chemistry.

Perhaps the most impressive strategy to create multinuclear complexes of exchange-coupled metal ions has been a so-called "building block" approach,[15,16] which relies on the use of small metal-centered molecular units together with capping ligands that serve to prevent the growth of extended structures. This approach has been especially productive for oxide- and cyanide-bridged complexes, many of which appear as few-atom replicas cut out by the capping ligands from the common structure types (e.g., the perovskite for oxides[17,18] or the Prussian blue for cyanides[19−22]).

The oxalate ($C_2O_4^{2-}$) anion is another effective bridging ligand to mediate magnetic exchange coupling between metal cations. A quick survey of the Cambridge Structural Database[23] (v. 2024.3.0) reveals more than 4,000 oxalate-bridged structures, about a quarter of which are discrete molecular (not extended) structures, while the majority are extended coordination polymers. However, when the search is made

Received: February 24, 2025
Revised: July 8, 2025
Accepted: July 8, 2025
Published: July 19, 2025

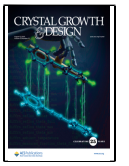

https://doi.org/10.1021/acs.cgd.5c00236
Cryst. Growth Des. 2025, 25, 5834−5844

more restrictive by requiring the structure to contain any metal center surrounded by three chelating and bridging oxalates, $[M(\mu\text{-}C_2O_4)_3]$, only 24 out of 690 hits are discrete molecular structures. Such a contrast, of course, is not surprising, keeping in mind that increasing the density of bridging oxalates should also encourage the formation of coordination polymers. It might also suggest the lack of systematic studies aimed at producing a larger variety of such complexes (Scheme 1).

Scheme 1. Chemical Structure of a Multinuclear Complex Centered by a Tris(oxalato)chromium(III) Unit (a) and its Topological Relationship to the α-$RuCl_3$ Type Structure (b)

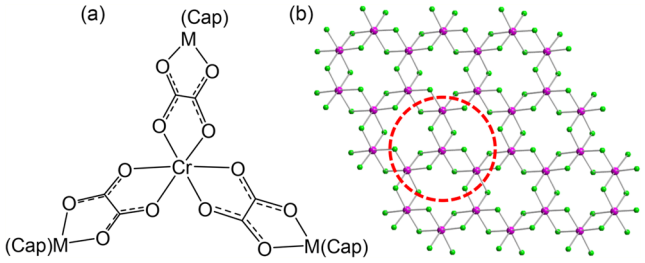

Oxalate-bridged frameworks of transition metal ions were broadly investigated due to the richness of their magnetic and catalytic properties.[24,25] In one of the most remarkable examples,[26] a two-dimensional (2D) anionic layer formed by oxalate-bridged Mn^{2+} and Cr^{3+} ions was cocrystallized with bis(ethylenedithio)tetrathiafulvalene (BEDT-TTF) cations to afford a hybrid material, $(BEDT\text{-}TTF)_3[MnCr(\mu\text{-}C_2O_4)_3]$, that showed coexistence of ferromagnetic ordering and metallic conductivity. Moreover, such 2D networks of oxalate-bridged metal ions are topologically equivalent to the structure of α-$RuCl_3$, which in recent years has been researched extensively by the condensed matter physics community as a prototype Kitaev system.[27] The latter represents a honeycomb lattice model, in which spin centers that appear in the three-connected nodes of the lattice exhibit anisotropic magnetic exchange interactions that lead to unique topological properties.[28]

Thus, the oxalate-bridged structures are of interest to a broad range of disciplines spanning materials science, physics and chemistry, which motivates us to expand the discovery and investigation of such structures at the level of discrete molecular complexes of oxalate-bridged metal ions, due to the scarcity of structurally characterized examples. Out of 24 CSD examples mentioned earlier, the majority contain a central lanthanide ion,[29,30] or sometimes a dimer of lanthanide ions,[31,32] connected to the peripheral metal ions through three or four bridging oxalates. A few of the examples contain a paramagnetic metal ion in the center surrounded by diamagnetic peripheral metal ions.[33,34] However, nearly all reported molecular structures that contain oxalate-bridged magnetically coupled metal ions were assembled with a central 3d or 4f metal and peripheral 4d or 5d metals (Ru, Re, Os) terminated with chloride or bromide ligands.[29,30,35−37] Thus, it is the inertness of the 4d and 5d metals, rather than the use of capping ligands, that served as a factor preventing the growth of extended structures. Such an approach is problematic with much more labile 3d metal ions; therefore, the assembly of similar complexes containing only metals of the first transition row will require the use of capping ligands.

Herein, we report the synthesis, structure, and magnetism of a tetranuclear complex $[Ni_3(cyclen)_3Cr(\mu\text{-}C_2O_4)_3](ClO_4)_3$ (**1**), in which the central $[Cr(C_2O_4)_3]^{3-}$ unit is capped by three $[Ni(cyclen)]^{2+}$ fragments (cyclen = 1,4,7,10-tetraazacyclododecane). To the best of our knowledge, and somewhat surprisingly, this is the first example of an established crystal structure that contains the Ni^{2+} and Cr^{3+} ions bridged by the oxalate ligand, although a similar complex, without structural characterization, was reported by Pei et al.[38] We demonstrate that the complex exhibits an $S = 9/2$ ground state due to ferromagnetic exchange between the Ni^{2+} and Cr^{3+} centers but lacks substantial magnetic anisotropy. Nevertheless, it provides a valid structural model toward further development of mimics to study Kitaev-type interactions localized to a finite molecular unit.

MATERIALS AND METHODS

Starting Materials. All reactions were performed under open-air conditions. Commercial-grade methanol, ethanol, diethyl ether (all >99%, VWR), and acetonitrile (>99.5%, JT Baker), and the precursors $K_2Cr_2O_7$ (>99%, Sigma-Aldrich), $K_2C_2O_4{\cdot}H_2O$ (98%, Thomas Scientific), oxalic acid (>98%), 18-crown-6 (>99%), $Ni(ClO_4)_2{\cdot}6H_2O$ (99%), and cyclen (>98%, all from VWR) were used as received. $[Ni(cyclen)(MeCN)_2](ClO_4)_2$ and $K_3[Cr(C_2O_4)_3]{\cdot}3H_2O$ were synthesized according to the reported procedures (see Supporting Information). Elemental analyses were performed by Atlantic Microlab Inc. (Norcross, GA). *Caution! The complexes between metal ions and organic ligands with perchlorate counter ions are potentially explosive. The compounds should be prepared in small amounts and handled with great care!*

$[Ni_3(cyclen)_3Cr(\mu\text{-}C_2O_4)_3](ClO_4)_3$ (1). $K_3[Cr(C_2O_4)_3]{\cdot}3H_2O$ (48.7 mg, 0.100 mmol) and 18-crown-6 (81.9 mg, 0.310 mmol) were dissolved in 8 mL of acetonitrile (MeCN). (The use of 18-crown-6 is necessary to solubilize the potassium salt in MeCN.) To this solution was added a violet solution of $[Ni(cyclen)(MeCN)_2](ClO_4)_2$ (153 mg, 0.300 mmol) in 4 mL of MeCN, and the mixture was stirred for 10 min. The resulting light-violet solution was filtered and transferred into a glass tube of 4 mm inner diameter. Crystallization was achieved by diffusing diethyl ether (Et_2O) into the solution of the product. After 4 days, violet block-shaped crystals were isolated by filtration, washed successively with cold MeCN and Et_2O, and air-dried. Yield = 88.9 mg (68%). *Elem. Anal.* (%): Calcd (Found) for $Ni_3CrCl_3O_{28}N_{12}C_{30}H_{68}$ (**1**·$4H_2O$) C, 26.12 (26.47); H, 4.97 (5.02); Cl, 7.71 (7.21); N, 12.19 (12.14).

Physical Property Measurements. Fourier-transform infrared (FT-IR) spectra were recorded on a JASCO 6800 FT-IR spectrometer in the 250−4000 cm^{-1} range using a universal attenuated-total-reflection accessory. Thermogravimetric analysis (TGA) was performed on a TGA-550 thermogravimetric analyzer (TA Instruments) under a continuous flow of argon gas, in the range from room temperature to 600 °C at a heating rate of 10 °C/min.

X-ray Diffraction. Powder X-ray diffraction was performed at 295 K on a Rigaku SmartLab diffractometer equipped with a Cu-K_α source. The data were collected in the range of 5−30° with a step of 0.02° and a collection time of 1 h.

Single-crystal X-ray diffraction was performed on a Rigaku-Oxford Diffraction Synergy-S diffractometer equipped with a HyPix detector and a monochromated Mo-Kα (λ = 0.71073 Å) radiation source. A chosen single crystal was suspended in Parabar oil (Hampton Research) and mounted on a nylon loop, which was placed directly into the cold stream of N_2 gas to flash-cool the sample to 212 K. The data were collected as a series of ω-scans with a 0.5° step and integrated with the CrysAlis software package, which was also used for space group determination.[39] An empirical absorption correction was applied based on spherical harmonics as implemented in the SCALE3 ABSPACK algorithm.[40] The crystal structure solution and refinement were carried out with SHELX[41] using the Olex2 GUI.[42] The final refinement was performed with anisotropic atomic displacement

https://doi.org/10.1021/acs.cgd.5c00236
Cryst. Growth Des. 2025, 25, 5834−5844

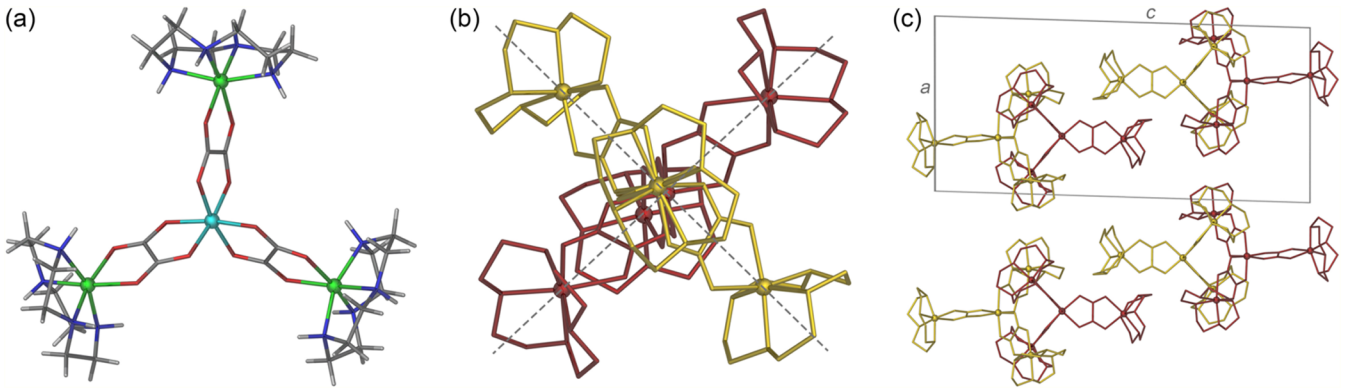

Figure 1. (a) One of the tetranuclear cations $[Ni_3(cyclen)_3Cr(\mu\text{-}C_2O_4)_3]^{3+}$ in the asymmetric unit of **1a**. Color scheme: Ni = green, Cr = cyan, O = red, *N* = blue, C = gray, H = off-white. (b) The view of the two tetranuclear cations, distinguished by garnet and gold colors, in the asymmetric unit of **1a**. The H atoms are omitted for clarity. The Ni and Cr metal centers are emphasized as spheres, to visualize approximate planes (indicated with dashed gray lines) that contain these metal ions in each cationic complex. The angle between the planes is 87.1°. (c) The crystal packing of **1a** viewed down the *b* axis. The two crystallographically distinct tetranuclear complexes are emphasized by different colors. The unit cell *a* and *c* axes are also indicated. The ClO_4^- anions and crystallization solvent molecules are omitted for clarity.

parameters (ADPs) for all non-hydrogen atoms, except for one severely disordered perchlorate ion and a water molecule that were treated isotropically. All H atoms were placed in calculated positions and refined in the riding model. In addition, a substantial disordered electron density, detected in two voids in the crystal structure, was treated with a solvent mask procedure as implemented in Olex2,[42] which revealed the presence of ∼ 1.5 additional disordered MeCN molecules per formula unit. Full details of the crystal structure refinement and the final structural parameters have been deposited with the Cambridge Crystallographic Data Centre (CCDC). The CCDC registry number and a summary of data collection and refinement parameters are provided in Table S1.

The Hirshfeld surface analysis was performed using the freely available Crystal Explorer software, which also was used to create the plots of Hirshfeld surfaces, intermolecular contact histograms, and two-dimensional fingerprint plots of intermolecular interactions.[43]

Magnetic Measurements. Magnetic measurements were performed using a magnetic property measurement system MPMS-3 (Quantum Design) equipped with a superconducting quantum interference device (SQUID). For each measurement, the sample was loaded in a polycarbonate capsule that was mounted in a plastic straw attached to a sample transport rod. The temperature dependence of magnetic susceptibility was measured in the range of 1.8−300 K in an applied field of 1000 Oe at a rate of 2 K/min. Field-dependent magnetization was measured at 1.8 K with the magnetic field varying from 0 to 70 kOe. The data were corrected for diamagnetism from the sample holder and for intrinsic diamagnetism using tabulated constants.[44] The fitting of the magnetic data was performed with the PHI software.[45]

Computational Details. DFT calculations were performed using the Vienna Ab initio Simulation Package[46] version 6.3.2. The projector augmented wave (PAW) pseudopotentials[47] based on the Perdew−Burke−Ernzerhof (PBE) exchange-correlation energy density functional[48] were used. Both the PBE exchange-correlation energy density functional and the Heyd-Scuseria-Ernzerhof (HSE06) hybrid exchange-correlation energy density functional, as revised by Krukau et al.,[49] were applied. The energy cutoff for plane waves was set to 600 eV. The energy tolerance was set to 1×10^{-8} eV. A vacuum of at least 12 Å was added around the molecule to reduce the interaction between periodic images. The molecular geometry was taken from the experimentally determined crystal structure and kept fixed in our calculations. When the PBE exchange-correlation energy density functional was applied, we used the DFT+*U* method by Dudarev et al.[50] for the 3d orbitals of transition metal elements to account for the correlation energy beyond the exchange-correlation energy density functional. The on-site Coulomb interaction parameter *U* was set to 3.00 eV for Ni and 1.24 eV for Cr, based on literature reports.[51−53] These values of *U* were not tuned to match the experimental observations.

State-average CASSCF calculations were performed on model cationic complexes, $[NiZn_2(cyclen)_3Sc(\mu\text{-}C_2O_4)_3]^{3+}$ ($NiZn_2Sc$) and $[Zn_3(cyclen)_3Cr(\mu\text{-}C_2O_4)_3]^{3+}$ (Zn_3Cr), using the ORCA package,[54] version 5.0.4, using the experimental atomic positions as determined by X-ray diffraction. The active space was chosen to be (8e, 10o) (eight electrons in ten active orbitals) for $NiZn_2Sc$ and (3e, 10o) for Zn_3Cr. The def2-TZVP basis set together with the def2/JK auxiliary basis sets were adopted for all the elements.[55,56] The resolution of identity approximation was applied to accelerate the calculations.[57−59] The convergence tolerances for energy and orbital gradient were set to 2.5×10^{-8} E_h and 2.5×10^{-4}, respectively. Dynamical correlation beyond the active space was included via the strongly contracted second-order N-electron valence state perturbation theory (NEVPT2)[60−63] after the self-consistent conditions were achieved in the CASSCF calculation. The spin−orbit interaction was treated by the spin−orbit mean field approximation[64] and the quasi-degenerate perturbation theory (QDPT).[65,66] The zero-field splitting (ZFS) parameters as well as the Landé g-factors were calculated by the pseudospin Hamiltonian approach using the SINGLE_ANISO program.[67,68]

High-Field Electron Paramagnetic Resonance (HF-EPR) Spectroscopy. HF-EPR measurements were performed between 63 and 379 GHz in the temperature range of 5−150 K, using a home-built spectrometer at the National High Magnetic Field Laboratory's EMR facility. The transmission-type spectrometer utilized cylindrical light pipes to propagate microwaves to and from the sample. Microwaves were generated by a phase-locked source with a 13.1 ± 1 GHz base frequency, followed by a solid-state multiplier chain (Virginia Diodes, Inc., Charlottesville, VA). Signal detection was carried out using an InSb hot-electron bolometer (QMC Instruments Ltd., Cardiff, U.K.), and a lock-in amplifier (Stanford Research Systems, Sunnyvale, CA) was used to convert the field-modulated signal into a DC voltage for analysis. A superconducting magnet (Oxford Instruments plc, U.K.) provided magnetic fields up to 14.5 T. EPR spectral simulations were carried out using EasySpin v. 6.0.6.[69]

RESULTS AND DISCUSSION

Synthesis. The assembly of the tetranuclear complex **1** relies on the bridging nature of the chelating $C_2O_4^{2-}$ ligands and the blocking action of the tetradentate cyclen ligands, which prevent the growth of an extended structure. Both the starting materials and the product are highly soluble in MeCN; thus, the crystallization of **1** was induced by diffusion of Et_2O into the solution of the complex. The large violet block-like

https://doi.org/10.1021/acs.cgd.5c00236
Cryst. Growth Des. 2025, 25, 5834−5844

crystals had the composition **1**·6.5MeCN·0.5H_2O (**1a**), according to the X-ray crystal structure determination (see below), while the powder sample, which was dried under suction and then handled in air, had the composition **1**·4H_2O (**1b**) determined by elemental analysis. The FT-IR spectrum of **1b** showed a characteristic peak at 1645 cm^{-1} (Figure S1), corresponding to the stretching mode of the bridging $C_2O_4^{2-}$ ligand.[70,71] TGA performed on a suction-dried sample showed an initial mass decrease of ∼5% when the sample was heated to 100 °C. This change corresponds to a loss of ∼ 3.8 water molecules per tetranuclear complex, which is in a very good agreement with the results of elemental analysis for **1b**. Decomposition of the sample, most likely due to the explosive nature of the perchlorate complex, was observed when heated above 300 °C (Figure S2).

Crystal Structure. Crystal structure determination from single-crystal X-ray diffraction data revealed that complex **1** crystallizes in the space group $P\bar{1}$. The asymmetric unit contains two $[Ni_3(cyclen)_3Cr(\mu\text{-}C_2O_4)_3]^{3+}$ cations, six ClO_4^- anions, 13 MeCN molecules, and one H_2O molecule, giving $[Ni_3(cyclen)_3Cr(\mu\text{-}C_2O_4)_3](ClO_4)_3$·6.5MeCN·0.5$H_2O$ (**1a**) as the full formula unit. In each cationic complex (Figure 1a), three bridging oxalate ligands connect the central Cr^{3+} ion to the three peripheral Ni^{2+} ions capped by cyclen ligands. All metal centers are in a distorted octahedral geometry. Each Cr^{3+} ion is surrounded by six oxygen atoms of the three bridging and chelating oxalate ligands, while each Ni^{2+} ion is surrounded by four nitrogen atoms of the capping cyclen ligand and two oxygen atoms of one oxalate ligand. The Cr−O distances range from 1.965(3) to 1.989(5) Å, while the Ni−O and Ni−N distances show slightly larger variation, from 2.090(3) to 2.130(3) Å and from 2.022(6) to 2.116(5) Å, respectively (Table 1). These distances are in close agreement with the reported distances for the Cr^{3+} and Ni^{2+} ions found in similar coordination environments (see Table S2). The interatomic Cr···Ni distances within the complex vary from 5.2917(10) to 5.3385(9) Å, while the nearest interatomic distance between the two crystallographically unique Cr^{3+} centers is 5.3235(9) Å. The Ni−Cr−Ni angles vary from 107.11 to 130.39° (Table 1). The sum of these angles equals 360° for each of the tetranuclear clusters in the asymmetric unit, indicating that in each cluster the three Ni^{2+} and one Cr^{3+} ion reside in the same plane (Table 1).

In each tetranuclear complex, the Ni^{2+} ions thus form a triangle centered by the Cr^{3+} ion, with all four atoms residing in the same plane. The mean-square deviation from the common plane is 0.0097 Å and 0.0124 Å for the two cationic complexes found in the asymmetric unit. These two planes are at 87.1° to each other (Figure 1b). A view of the crystal packing of **1a** down the *b* axis (Figure 1c) reveals clearly how the crystallographically distinct tetranuclear complexes are arranged in the lattice. Such packing of the cationic units leaves large lattice voids, which are filled by the ClO_4^- anions and crystallization solvent molecules (Figure S3).

To analyze the intermolecular interactions in the structure of **1a**, we carried out the Hirshfeld surface analysis.[72] The calculated surface is shown in Figure 2, where blue and white regions represent the contacts with interatomic distances greater than or similar to the sum of the van der Waals radii between the corresponding atoms. The red regions emphasize shorter contacts that are below the sum of the van der Waals radii. As can be seen from this analysis, there are a few such red regions that mainly emerge as strong hydrogen bonding

Table 1. Interatomic Distances and Selected Angles in the Crystal Structure of 1a

d(Cr−O), Å		d(Ni−O), Å	
Cr1−O1	1.977(3)	Ni1−O7	2.090(3)
Cr1−O2	1.977(3)	Ni1−O8	2.130(3)
Cr1−O3	1.965(3)	Ni2−O9	2.113(4)
Cr1−O4	1.976(3)	Ni2−O10	2.106(3)
Cr1−O5	1.982(3)	Ni3−O11	2.107(3)
Cr1−O6	1.989(5)	Ni3−O12	2.111(3)
Cr2−O13	1.985(3)	Ni4−O19	2.120(3)
Cr2−O14	1.976(3)	Ni4−O20	2.110(3)
Cr2−O15	1.969(3)	Ni5−O23	2.096(4)
Cr2−O16	1.978(3)	Ni5−O24	2.138(4)
Cr2−O17	1.966(3)	Ni6−O21	2.092(3)
Cr2−O18	1.986(3)	Ni6−O22	2.108(3)
d(Ni−N), Å			
Ni1−N1	2.044(5)	Ni4−N13	2.058(4)
Ni1−N2	2.110(6)	Ni4−N14	2.116(5)
Ni1−N3	2.055(5)	Ni4−N15	2.050(5)
Ni1−N4	2.108(5)	Ni4−N16	2.083(4)
Ni2−N5	2.059(5)	Ni5−N17	2.087(5)
Ni2−N6	2.095(4)	Ni5−N18	2.058(4)
Ni2−N7	2.042(5)	Ni5−N19	2.082(4)
Ni2−N8	2.081(4)	Ni5−N20	2.038(5)
Ni3−N9	2.022(4)	Ni6−N21	2.063(6)
Ni3−N10	2.061(5)	Ni6−N22	2.112(7)
Ni3−N11	2.088(5)	Ni6−N23	2.021(4)
Ni3−N12	2.085(4)	Ni6−N24	2.092(7)
d(Cr···Ni), Å		angles (deg)	
Cr1···Ni1	5.3381(8)	Ni1−Cr1−Ni2	114.41(1)
Cr1···Ni2	5.3097(8)	Ni2−Cr1−Ni3	124.84(1)
Cr1···Ni3	5.3510(8)	Ni3−Cr1−Ni1	120.75(1)
Cr2···Ni4	5.3360(8)	Ni4−Cr2−Ni5	122.50(2)
Cr2···Ni5	5.3369(8)	Ni5−Cr2−Ni6	130.39(2)
Cr2···Ni6	5.2919(9)	Ni6−Cr2−Ni4	107.11(1)

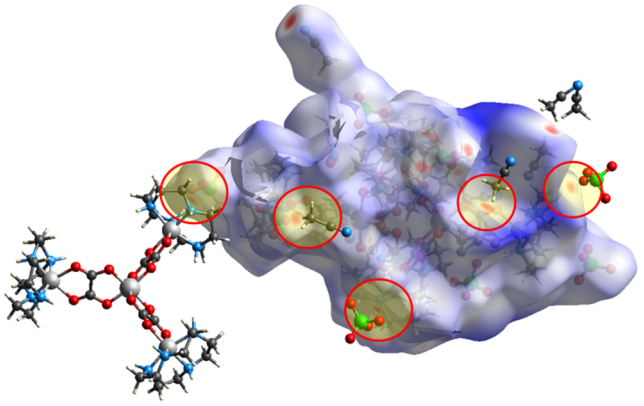

Figure 2. Hirshfeld surface calculated for the crystal structure of **1a**. The highlighted red spots indicate significant hydrogen bonding as discussed in the text.

formed by the ClO_4^- anions, as well as hydrogen bonding between the N−H group of the cyclen ligand and the MeCN molecules. Thus, these hydrogen bonding interactions play the major role in stabilizing the crystal packing of **1a**, accounting for ∼47% of all intermolecular contacts (Figures S4 and S5). Nevertheless, they are not strong enough to prevent the loss of crystallinity when the crystals are exposed to air.

https://doi.org/10.1021/acs.cgd.5c00236
Cryst. Growth Des. 2025, 25, 5834−5844

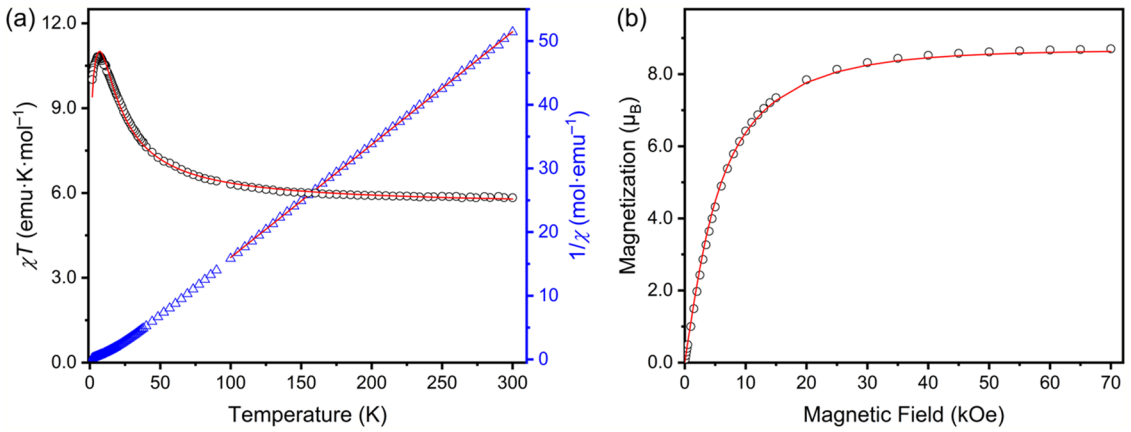

Figure 3. Temperature dependence of χT and $1/\chi$ measured under applied field of 1000 Oe (a) and field dependence of magnetization measured at 1.8 K (b) on a powder sample of **1b**. The solid red lines show the theoretical fits described in the main text.

The open nature of the large voids in the crystal packing of **1a** explains the facile loss of MeCN molecules and their replacement with atmospheric water when the material is suction-dried. Despite this solvent replacement, established by the elemental analysis and indirectly corroborated by the TGA analysis, the conversion from **1a** to **1b**, through the loss of the interstitial MeCN molecules, leads to the loss of crystallinity. Powder X-ray diffraction measurements revealed that the dried crystals of **1a** maintain the semicrystalline nature (Figure S6) but grinding them to powder leads to the loss of the long-range structural order in sample **1b**. Importantly, however, the integrity of the tetranuclear complexes is preserved, as indicated by identical "fingerprint" IR spectra obtained for the dried crystals and powder sample. In both cases, we observed the prominent peak at 1645 cm^{-1} characteristic of the bridging oxalate ligand (Figure S1). Therefore, the change from the crystalline sample to the powder sample should have a negligible impact on the interpretation of magnetic and EPR data described below, since the magnetic interactions are dominated by the intramolecular magnetic exchange mediated by the $C_2O_4^{2-}$ ligands that bridge the Ni^{2+} and Cr^{3+} ions within the same tetranuclear unit.

Magnetic Properties. *Magnetometry.* Temperature-dependent magnetic susceptibility (χ) was measured on an air-dried powder sample of **1b**. The χT product increases from the value of 5.84 emu·K·mol^{-1} at 300 K to the maximum of 10.82 emu·K·mol^{-1} at 7.2 K, after which it drops to the value of 10.01 emu·K·mol^{-1} at 1.8 K (Figure 3a). Such behavior is indicative of ferromagnetic exchange coupling between three Ni^{2+} (S = 1) and one Cr^{3+} (S = 3/2) ions. The temperature dependence of $1/\chi$ was fit to the Curie–Weiss law, $1/\chi = (T - \theta)/C$, yielding the best-fit values of the Curie and Weiss constants, C = 5.643(9) emu·K·mol^{-1} and θ = 9.5(3) K, respectively (R^2 = 0.9999). The positive value of θ is in agreement with the ferromagnetic exchange between the metal ions. The value of C is notably higher than the spin-only value of 4.875 emu·K·mol^{-1} calculated for the system of three Ni^{2+} and one Cr^{3+} ions in the absence of magnetic exchange. This difference can be explained by the orbital contribution to the magnetic moment of the Ni^{2+} ions.

Next, the temperature dependence of χT was fit by using the Heisenberg-Dirac-Van Vleck Hamiltonian,

$$\hat{\mathcal{H}} = -2J\sum_{k=1}^{3}\hat{S}_{Cr}\cdot\hat{S}_{Ni}^{k} + 3D_{Ni}\left[\hat{S}_{z,Ni}^{2} - \frac{1}{3}S_{Ni}(S_{Ni}+1)\right] + \mu_B(g_{Cr}\hat{S}_{Cr} + 3g_{Ni}\hat{S}_{Ni})\cdot\vec{B} \quad (1)$$

where J is the magnetic exchange constant, $\hat{S}_{Cr}$ and $\hat{S}_{Ni}$ are the spin operators and g_{Cr} and g_{Ni} are the Landé g-factors of the corresponding metal ions, D_{Ni} is the single-ion axial ZFS parameter for each Ni^{2+} ion, μ_B is the Bohr magneton, and B is the applied magnetic field. The value of g_{Cr} was fixed to 2.0099, using the value determined for $K_3[Cr(C_2O_4)_3]\cdot 3H_2O$ (see Supporting Information, Figure S7). Then the χT data were fit with the PHI software, giving the best-fit values of J = +3.45(3) cm^{-1}, D_{Ni} = +4.83(3) cm^{-1}, and g_{Ni} = 2.196(5) (R^2 = 0.9980). These spin Hamiltonian parameters derived by fitting the χT data will be compared with the calculated values in the Theoretical Studies section. [We would like to point out that performing such measurements on the dried crystals that were not crushed to powder produced essentially identical results (Figure S8), suggesting that the integrity of the tetranuclear complexes and intramolecular exchange interactions between the Ni^{2+} and Cr^{3+} ions are not compromised by the loss of crystallinity.]

Consistent with previous literature reports of discrete molecular clusters in which the Ni^{2+} and Cr^{3+} ions are connected by a short diamagnetic bridge (Table 2), we observed ferromagnetic exchange coupling between these ions. For a more comprehensive account of such interactions, we refer a reader to the topical review.[25]

The ferromagnetic exchange between the three Ni^{2+} and one Cr^{3+} ion should lead to a ground state with spin, S = 9/2, which was probed by measuring a field-dependent magnetization isotherm at 1.8 K. The magnetization reached the maximum value of 8.70 μ_B, which is in good agreement with the theoretical value of 9.0 μ_B expected for the S = 9/2 ground state (Figure 3b). To determine the magnetic parameters of the ground spin state, isothermal magnetization (M) curves were measured for complex **1b** in the 1.8–4.2 K temperature range, with the applied field varying from 0 to 70 kOe. The reduced magnetization data, plotted as M vs B/T (Figure S9), were simulated with the PHI software for the S = 9/2 ground state with Hamiltonian (2),

$$\hat{\mathcal{H}} = g\mu_B\hat{S}\cdot\vec{B} + D\left[\hat{S}_z^2 - \frac{1}{3}S(S+1)\right] \quad (2)$$

https://doi.org/10.1021/acs.cgd.5c00236
Cryst. Growth Des. 2025, 25, 5834–5844

Table 2. Comparison of Magnetic Exchange Constants (J) between Ni^{2+} and Cr^{3+} Ions in Discrete Multinuclear Molecular Complexes

compound[a]	bridge	J (cm^{-1})[b]
$[\{Ni(Me_6\text{-}[14]ane\text{-}N_4)\}_3Cr(\mu\text{-}C_2O_4)_3](ClO_4)_3$	μ-C_2O_4	+10.6[38]
$[(NiL)_3Cr(\mu\text{-}C_2O_2S_2)_3](ClO_4)_3$	μ-$C_2O_2S_2$	+5.9[73]
$[\{Ni\text{-}(iPrtacn)Cl\}_3BztacnCr(CN)_3]Cl_3\cdot 10H_2O$	CN	+40[74]
$[\{Ni(Me_2valpn)\}_2Y(H_2O)Cr(CN)_6]$	CN	+9.4[75]
Complex 1 (this work)	μ-C_2O_4	+3.45

[a]Me_6-[14]ane-N_4 = 5,7,7,12,14,14-hexamethyl-1,4,8,11-tetraaza-cyclotetradecane; L = 5,5,7,12,12,14-hexamethyl- 1,4,8,11-tetraaza-cyclotetradecane; Bztacn = 1,4,7-trisbenzyl-1,4,7-triaza-cyclononane, iPrtacn = 1,4,7-trisisopropyl-1,4,7-triaza-cyclononane. [b]All magnetic exchange constant values have been converted to the $-2J$ convention used in Hamiltonian (1).

giving the best-fit parameters g = 1.95 and $|D|$ = 0.22 cm^{-1} (note that both positive and negative values of D gave a satisfactory fit to the experimental data). The small value of D contrasts with the significant ZFS anisotropy with D = +2.08 cm^{-1} established for the model mononuclear complex $[Ni(cyclen)(MeCN)_2]^{2+}$ (Figure S10). This difference is explained by the dilution of the single-ion anisotropy due to (i) the local molecular frames of the Ni^{2+} ions being at 120° to one another in the tetranuclear cluster, (ii) the Cr^{3+} ion contributing negligible overall anisotropy to the coupled spin system, and (iii) the overall single-ion anisotropy being projected onto a large total ground-state spin of S = 9/2, which decreases the projected D value by a factor of $1/S$.[76] This conclusion is further corroborated by the theoretical and EPR studies described below.

Theoretical Studies. To obtain the spin Hamiltonian parameters for a Ni^{2+} ion, we replaced the other Ni^{2+} ions by diamagnetic Zn^{2+} ions and the central Cr^{3+} ion by a diamagnetic Sc^{3+} ion, thus creating a model tetranuclear cluster $NiZn_2Sc$. Since the three Ni^{2+} ions are in nearly the same chemical environment, we calculated the ZFS parameters for only one of the Ni^{2+} sites. In the same manner, to obtain the spin Hamiltonian parameters for the Cr^{3+} ion, we replaced all the Ni^{2+} ions by Zn^{2+} ions to create a model cluster Zn_3Cr. Figure 4a shows the five molecular orbitals with 3d character associated with Ni from the CASSCF calculation of $NiZn_2Sc$. The energies of these 3d orbitals were evaluated using the lowest-energy spin-free root, and they are given in the upper part of Table 3. As expected, these orbitals form nearly degenerate orbital triplet and doublet sets which are separated by an energy gap of more than 10 eV. Note that, due to the nature of CASSCF theory, this energy gap differs from the crystal field splitting parameter in ligand field theory. An analysis using the ab initio ligand field theory[77,78] yields a crystal field splitting parameter of ~1.074 eV (~8660 cm^{-1}) for the Ni^{2+} ion based on the same set of 3d orbitals.

Figure 4b shows the molecular orbitals with 3d character around Cr from the CASSCF calculation of Zn_3Cr. The energies of these 3d orbitals are given in the lower part of Table 3. Again, the orbitals split into the nearly degenerate 3-fold and 2-fold levels, with the crystal field splitting parameter of ~1.952 eV (~15740 cm^{-1}) for the Cr^{3+} ion according to the ab initio ligand field theory. The occupation numbers of the molecular orbitals in the ground state (without the spin−orbit coupling) are also given in Table 3. The Ni and Cr atoms retain almost eight and three 3d electrons, respectively, in agreement with the +2 and +3 charges of these ions.

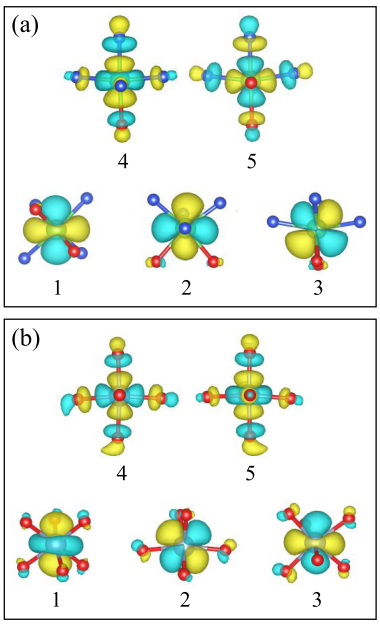

Figure 4. Active molecular orbitals with 3d orbital character for (a) $NiZn_2Sc$ and (b) Zn_3Cr, as obtained by CASSCF calculations. The isosurface value was set to ± 0.02 and ± 0.03 $Bohr^{-3/2}$ for the Ni and Cr sites, respectively. The positive and negative values are indicated with yellow and cyan, respectively. The orbital energy increases with the orbital index that is marked below the orbitals. The N and O atoms are shown with blue and red colors, respectively.

Table 3. Energies and Occupation Numbers of the Molecular Orbitals Shown in Figure 4[a]

$NiZn_2Sc$					
orbital index	1	2	3	4	5
energy (eV)	−22.81	−22.78	−22.71	−9.75	−9.72
occupancy	1.989	1.988	1.989	0.996	0.996
Zn_3Cr					
orbital index	1	2	3	4	5
energy (eV)	−10.28	−10.27	−10.26	+1.56	+1.58
occupancy	0.998	0.998	0.998	0.000	0.000

[a]The values were obtained for the lowest-energy spin-free root that has S = 1 for $NiZn_2Sc$ and S = 3/2 for Zn_3Cr.

To further investigate the nature of magnetic exchange in complex **1**, we generalized the single isotropic exchange coupling constant in eq 1 to three independent matrices, each of which is for one Cr−Ni pair, and calculated the exchange coupling matrices using DFT. As shown in Table 4, the exchange coupling is nearly isotropic for all three Cr−Ni pairs, corroborating the high quality of the fit of the measured magnetic susceptibility using an isotropic exchange interaction, and being in agreement with the well-known isotropic behavior of the octahedrally coordinated Cr^{3+} ion. The average of the diagonal matrix elements of the exchange coupling matrix, J_{iso}, is 13.44, 13.01, and 12.60 cm^{-1} for the three Cr−Ni pairs using PBE+U. The variation of J_{iso} across the three pairs is within 3.3% compared with the average value. The exchange coupling matrix for one of the pairs was also calculated using the hybrid functional HSE06, and the exchange coupling matrix is more isotropic compared to the PBE+U result. The corresponding J_{iso} = 8.56 cm^{-1} is closer to the experimental value of 3.45 cm^{-1}

https://doi.org/10.1021/acs.cgd.5c00236
Cryst. Growth Des. 2025, 25, 5834−5844

Table 4. Exchange Coupling Matrices Calculated by DFT for Different Ni−Cr Pairs[a]

pair	PBE+U	HSE06
Cr−Ni1	$\begin{pmatrix} 13.50 & 0.02 & 0.33 \\ -0.02 & 13.49 & 0.27 \\ 0.02 & -0.02 & 13.32 \end{pmatrix}$	$\begin{pmatrix} 8.58 & 0.01 & 0.09 \\ -0.01 & 8.57 & 0.06 \\ 0.01 & -0.01 & 8.53 \end{pmatrix}$
Cr−Ni2	$\begin{pmatrix} 13.09 & 0.00 & 0.44 \\ 0.00 & 13.07 & 0.29 \\ -0.08 & -0.02 & 12.88 \end{pmatrix}$	
Cr−Ni3	$\begin{pmatrix} 12.68 & -0.05 & 0.28 \\ 0.06 & 12.65 & 0.30 \\ 0.07 & -0.01 & 12.46 \end{pmatrix}$	

[a]PBE and HSE06 are two density functionals. The unit for the exchange coupling matrix is cm^{-1}.

than the PBE+U result. However, the J_{iso} calculated with HSE06 is still 2.5 times larger than the value obtained by simulating the experimental data. Such a large difference is likely caused by inaccurate mapping between the (fictitious) DFT wave functions and the spin states within the spin model. The calculations do agree with the experiment on the ferromagnetic nature of the exchange coupling between the Ni^{2+} and Cr^{3+} ions. (The energy density functional HSE06 was applied for only one Ni−Cr pair since the variation in J_{iso} is small and hybrid functional calculations are computationally heavy.)

The ZFS parameters calculated by both DFT and CASSCF are given in Tables 5 and S4. The ZFS parameter for the Ni^{2+} ion is negative by DFT but positive by CASSCF. The latter gave D = +1.94 cm^{-1}, which is consistent with the experimental value of +2.08 cm^{-1} (Table S3) obtained for $[Ni(cyclen)(MeCN)_2](ClO_4)_2$, both in the sign and magnitude and, thus, the Ni^{2+} ion should have a magnetic easy plane. There is a sizable angle of 26.4° between the magnetic easy plane of the Ni^{2+} ion and the plane formed by the three Ni^{2+} ions. The misalignment between these two planes slightly dilutes the magnetic anisotropy in the giant-spin model, as shown in Table S5. The same table shows that an order of magnitude smaller ZFS parameter D than the D_{Ni} in the giant-spin model is consistent with the multispin model. The orientation of the tensor frames for the calculated ZFS parameters and g-factors are provided in Table S6.

Table 5. Calculated Single-Ion ZFS Parameters and g Factors

Ni^{2+}	D (cm^{-1})	E (cm^{-1})	g_x	g_y	g_z
DFT	−3.92	−0.15			
CASSCF	+1.94	+0.09	2.238	2.245	2.252
Cr^{3+}	D (cm^{-1})	E (cm^{-1})	g_x	g_y	g_z
DFT	−4.58	−0.03			
CASSCF	−0.24	−0.03	1.963	1.963	1.961

The ZFS parameter D for Cr^{3+} is negative by both DFT and CASSCF indicating a magnetic easy axis for the Cr^{3+} ion, but the magnitude of D by CASSCF is 18 times smaller than that by DFT. Again, the CASSCF result of D = −0.24 cm^{-1} is closer to the experimental value of 0.359 cm^{-1} (the sign of D was not determined) reported for the model compound $K_2C_2O_4$.[79] The E/D ratio, which quantifies the in-plane anisotropy, equals 0.047 for the Ni^{2+} ion and 0.125 for the Cr^{3+} ion according to CASSCF calculations. The g-factors calculated by the pseudospin Hamiltonian approach are nearly isotropic for both Ni^{2+} and Cr^{3+} (Table 5).

HF-EPR Spectroscopy. To confirm the hypothesis about the dilution of magnetic anisotropies in the tetranuclear cluster, despite the presence of significant single-ion anisotropy for individual Ni^{2+} ions, we collected high-field EPR spectra on powder samples of **1b** and the model mononuclear fragment, $[Ni(cyclen)(MeCN)_2](ClO_4)_2$. The spectrum of the model complex (Figure S10) was successfully simulated with $(g_{x,y}, g_z)$ = (2.11, 2.20) and D = +2.08 cm^{-1} for the S = 1 state.

On the other hand, the simulation of HF-EPR spectra of multimetallic complexes is nontrivial due to additional complications caused by the presence of exchange interactions and more complex relationships between the orientations of the ZFS tensors of the individual metal ions. The higher dimensionality of the Hilbert space (i.e., $\Pi_i(2S_i + 1) = 108$ for complex **1**) requires expansive diagonalization. Moreover, D- and g-strain caused by disorder and thermal population of excited states due to the small J value can lead to substantial broadening of EPR spectra.[80] With these considerations in mind, we used the following Hamiltonian to simulate the multifrequency EPR spectra of **1** (Figure 5):

$$\hat{H} = -2J \sum_{i=1}^{3} \hat{S}_{Cr} \cdot \hat{S}^{i}_{Ni} + \sum_{i=1}^{3} \hat{S}^{i}_{Ni} \cdot \vec{\vec{R}}_i^{T} \cdot \vec{\vec{D}}_{Ni} \cdot \vec{\vec{R}}_i \cdot \hat{S}^{i}_{Ni} + \mu_B (g_{Cr} \hat{S}_{Cr} + 3 g_{Ni} \hat{S}_{Ni}) \cdot \vec{B} \quad (3)$$

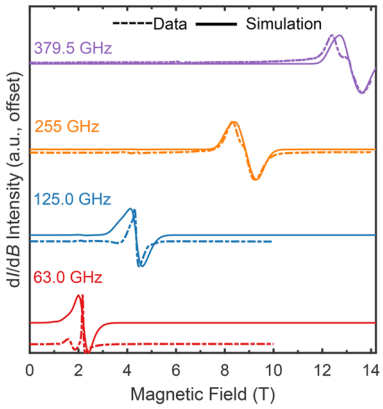

Figure 5. Continuous-wave, variable frequency EPR spectra of **1b** (dotted lines) and corresponding simulations (solid lines).

Like eq 3, the first and last terms respectively describe the coupling between the three Ni^{2+} ions with the Cr^{3+} ion and the individual Zeeman interactions. To simplify the model, we assume these interactions to be isotropic and identical for the three contacts and the three Ni^{2+} ions. Meanwhile, the second term parametrizes the ZFS interactions at the Ni^{2+} sites. We again assume the local tensors to be identical at each Ni^{2+} site, as specified by the traceless and axial diagonal matrix, $\vec{\vec{D}}_{Ni}$, with diagonal components $[-D/3, -D/3, +2D/3]$, i.e., we neglect local rhombic ZFS. We then rotate the individual tensors into the molecular frame via the Euler matrices, $\vec{\vec{R}}_i$ (ZYZ convention), where the superscript, T, denotes transpose in eq 3.

This model is significantly overparameterized. Consequently, many further assumptions are made in simulating the HF-EPR spectra. Our intent here is not to obtain perfect agreement, but to show that we can take realistic parameters obtained independently from other measurements and generate rather isotropic spectra for the coupled system. As stated already, the

https://doi.org/10.1021/acs.cgd.5c00236
Cryst. Growth Des. 2025, 25, 5834−5844

primary factors contributing to the weak anisotropy in the coupled system are the orientations of the individual Ni^{2+} ZFS tensors, which we assume to lie in a plane and at 120° to each other; and the dilution of the anisotropies of the constituent ions when projecting onto the total ferromagnetic $S = 9/2$ ground state, with negligible contribution from the Cr^{3+}.

To this end, for these simulations, we fixed J and D to the values deduced from the χT versus T fits (Figure 3) and the EPR measurements on the $[Ni(cyclen)(MeCN)_2](ClO_4)_2$ fragment (Figure S10), respectively. We set the isotropic Cr^{3+} g-factor to 2.00 and adjusted $g_{Ni} = 2.10$ so that the simulated spectra were centered on the experimental ones; again, g_{Ni} is assumed to be isotropic for the sake of simplicity. We then assumed identical Hamiltonians for the two molecules in the asymmetric unit, and a perfect 120° arrangement of the $\tilde{\boldsymbol{D}}_{Ni}$ tensors within each molecule. In addition, to reproduce the line shape of experimental EPR spectra we included a field-independent peak-to-peak line width (lwpp) of 250 mT, and a D-strain of 80 GHz. Here, D-strain accounts for a distribution in the axial ZFS parameter, D, due to structural variations in the Ni^{2+} ion coordination environment. Together, these two line broadening mechanisms serve as proxies for all of the factors that lead to degradation of the EPR spectra, and account for the fact that we do not resolve fine structures due to the individual transitions within the $S = 9/2$ manifold. Frequency-dependent simulations are displayed and superimposed on the experimental spectra in Figure 5. As can be seen, the peak-to-dip widths of the spectra span less than 2 T, compared to around 5 T in the model $[Ni(cyclen)(MeCN)_2](ClO_4)_2$ fragment (Figure S10), thus demonstrating the dilution of the anisotropy in the coupled system.

CONCLUDING REMARKS

This work demonstrates a successful design strategy to develop finite molecular systems that can mimic the local bonding topology of the honeycomb lattice model. The magnetic studies reveal that exchange coupling between the Cr^{3+} and Ni^{2+} ions is ferromagnetic and isotropic. Thus, while tetranuclear complex **1** opens the way toward the synthetic assembly of molecular complexes inspired by the Kitaev lattice model, the specific metal ions used in the present case do not reflect the pronounced anisotropic exchange that underlies the Kitaev physics. Our future efforts will focus on the use of more anisotropic central metal ions, such as low-spin Fe^{3+} and Ru^{3+}, to achieve anisotropic magnetic exchange coupling in the triangular complexes assembled with bridging oxalates or similar ligands.

ASSOCIATED CONTENT

Supporting Information

The Supporting Information is available free of charge at https://pubs.acs.org/doi/10.1021/acs.cgd.5c00236.

A summary of crystallographic data and bond lengths, an FT-IR spectrum and TGA curve of **1b**, 2D fingerprint plots and histograms of Hirshfeld surface analysis for **1a**, additional magnetic data for **1b** and $K_3[Cr(C_2O_4)_3]\cdot 3H_2O$, EPR data for $[Ni(cyclen)(MeCN)_2](ClO_4)_2$, and molecular geometry used in calculations (PDF)

Accession Codes

Deposition Number 2426144 contains the supplementary crystallographic data for this paper. These data can be obtained free of charge via the joint Cambridge Crystallographic Data Centre (CCDC) and Fachinformationszentrum Karlsruhe Access Structures service.

AUTHOR INFORMATION

Corresponding Authors

Stephen Hill − *Department of Physics, Florida State University, Tallahassee, Florida 32306, United States; National High Magnetic Field Laboratory, Florida State University, Tallahassee, Florida 32310, United States; Department of Chemistry and Biochemistry, Florida State University, Tallahassee, Florida 32306, United States;* orcid.org/0000-0001-6742-3620; Email: shill@magnet.fsu.edu

Hai-Ping Cheng − *Department of Physics, Northeastern University, Boston, Massachusetts 02115, United States*; Email: ha.cheng@northeastern.edu

Michael Shatruk − *Department of Chemistry and Biochemistry, Florida State University, Tallahassee, Florida 32306, United States;* orcid.org/0000-0002-2883-4694; Email: shatruk@chem.fsu.edu

Authors

Shubham Bisht − *Department of Chemistry and Biochemistry, Florida State University, Tallahassee, Florida 32306, United States*

Shuanglong Liu − *Department of Physics, Northeastern University, Boston, Massachusetts 02115, United States*

Kavipriya Thangavel − *National High Magnetic Field Laboratory, Florida State University, Tallahassee, Florida 32310, United States*

Dibya Jyoti Mondal − *Department of Chemistry and Biochemistry, Florida State University, Tallahassee, Florida 32306, United States;* orcid.org/0000-0002-6778-9339

Xinsong Lin − *Department of Chemistry and Biochemistry, Florida State University, Tallahassee, Florida 32306, United States*

Sandugash Yergeshbayeva − *Department of Chemistry and Biochemistry, Florida State University, Tallahassee, Florida 32306, United States*

Complete contact information is available at: https://pubs.acs.org/10.1021/acs.cgd.5c00236

Author Contributions

The manuscript was written through contributions of all authors. All authors have given approval to the final version of the manuscript.

Funding

This work is supported by the Center for Molecular Magnetic Quantum Materials (M2QM), an Energy Frontier Research Center funded by the US Department of Energy, Office of Science, Basic Energy Sciences under Award DE-SC0019330. The calculations employed resources of the University of Florida Research Computing as well as the National Energy Research Scientific Computing Center (NERSC), a U.S. Department of Energy Office of Science User Facility located at Lawrence Berkeley National Laboratory, operated under Contract No. DE-AC02-05CH11231 using NERSC award BES-ERCAP0027689. The Quantum Design MPMS-3 system used for magnetic measurements was acquired with support of the NSF MRI program (DMR-2216125).

Notes

The authors declare no competing financial interest.

■ ACKNOWLEDGMENTS

We gratefully acknowledge access to equipment provided by the X-ray Crystallography Center (FSU075000XRAY) and the Materials Characterization Laboratory (FSU075000MAC) at the Department of Chemistry and Biochemistry, Florida State University.

■ ABBREVIATIONS

CSD =Cambridge Structural Database; DFT =density-functional theory; EPR =electron paramagnetic resonance; FT-IR =Fourier-transform infrared; HSE =Heyd-Scuseria-Ernzerhof; PBE =Perdew−Burke−Ernzerhof; SMM =single-molecule magnet; SMT =single-molecule toroic; TGA =thermogravimetric analysis; ZFS =zero-field splitting

■ REFERENCES

(1) Coronado, E. Molecular Magnetism: From Chemical Design to Spin Control in Molecules, Materials and Devices. *Nat. Rev. Mater.* **2020**, *5*, 87−104.
(2) Christou, G.; Gatteschi, D.; Hendrickson, D. N.; Sessoli, R. Single-Molecule Magnets. *MRS Bull.* **2000**, *25*, 66−71.
(3) Milios, C. J.; Winpenny, R. E. P. Cluster-Based Single-Molecule Magnets. In *Molecular Nanomagnets and Related Phenomena*; Gao, S., Ed.; Springer: Berlin, Heidelberg, 2015; pp 1−109.
(4) Zabala-Lekuona, A.; Seco, J. M.; Colacio, E. Single-Molecule Magnets: From Mn_{12}-Ac to Dysprosium Metallocenes, a Travel in Time. *Coord. Chem. Rev.* **2021**, *441*, No. 213984.
(5) Nakano, M.; Oshio, H. Magnetic Anisotropies in Paramagnetic Polynuclear Metal Complexes. *Chem. Soc. Rev.* **2011**, *40*, 3239−3248.
(6) Sessoli, R.; Gatteschi, D.; Caneschi, A.; Novak, M. A. Magnetic Bistability in a Metal-Ion Cluster. *Nature* **1993**, *365*, 141−143.
(7) Sessoli, R.; Tsai, H. L.; Schake, A. R.; Wang, S.; Vincent, J. B.; Folting, K.; Gatteschi, D.; Christou, G.; Hendrickson, D. N. High-Spin Molecules: $[Mn_{12}O_{12}(O_2CR)_{16}(H_2O)_4]$. *J. Am. Chem. Soc.* **1993**, *115*, 1804−1816.
(8) Thomas, L.; Lionti, F.; Ballou, R.; Gatteschi, D.; Sessoli, R.; Barbara, B. Macroscopic Quantum Tunnelling of Magnetization in a Single Crystal of Nanomagnets. *Nature* **1996**, *383*, 145−147.
(9) Wernsdorfer, W.; Sessoli, R. Quantum Phase Interference and Parity Effects in Magnetic Molecular Clusters. *Science* **1999**, *284*, 133−135.
(10) Hill, S.; Edwards, R. S.; Aliaga-Alcalde, N.; Christou, G. Quantum Coherence in an Exchange-Coupled Dimer of Single-Molecule Magnets. *Science* **2003**, *302*, 1015−1018.
(11) Woodruff, D. N.; Winpenny, R. E.; Layfield, R. A. Lanthanide Single-Molecule Magnets. *Chem. Rev.* **2013**, *113*, 5110−5148.
(12) Murray, K. S. *Single Molecule Toroics*; Springer Cham: 2022.
(13) Ungur, L.; Lin, S.-Y.; Tang, J.; Chibotaru, L. F. Single-Molecule Toroics in Ising-Type Lanthanide Molecular Clusters. *Chem. Soc. Rev.* **2014**, *43*, 6894−6905.
(14) Kaemmerer, H.; Baniodeh, A.; Peng, Y.; Moreno-Pineda, E.; Schulze, M.; Anson, C. E.; Wernsdorfer, W.; Schnack, J.; Powell, A. K. Inorganic Approach to Stabilizing Nanoscale Toroidicity in a Tetraicosanuclear $Fe_{18}Dy_6$ Single Molecule Magnet. *J. Am. Chem. Soc.* **2020**, *142*, 14838−14842.
(15) Shatruk, M.; Avendano, C.; Dunbar, K. R. Cyanide-Bridged Complexes of Transition Metals: A Molecular Magnetism Perspective. *Prog. Inorg. Chem.* **2009**, *56*, 155−334.
(16) Pedersen, K. S.; Bendix, J.; Clérac, R. Single-Molecule Magnet Engineering: Building-Block Approaches. *Chem. Commun.* **2014**, *50*, 4396−4415.
(17) Thuijs, A. E.; Li, X.-G.; Wang, Y.-P.; Abboud, K. A.; Zhang, X. G.; Cheng, H.-P.; Christou, G. Molecular Analogue of the Perovskite Repeating Unit and Evidence for Direct Mn^{III}-Ce^{IV}-Mn^{III} Exchange Coupling Pathway. *Nat. Commun.* **2017**, *8*, No. 500.
(18) Cao, T. S.; Chen, D.-T.; Abboud, K. A.; Zhang, X.; Cheng, H.-P.; Christou, G. Feasibility of Ground State Spin Switching in a Molecular Analogue of the Mixed-Metal Oxides with the Perovskite Structure. *Polyhedron* **2020**, *176*, No. 114275.
(19) Shatruk, M.; Dragulescu-Andrasi, A.; Chambers, K. E.; Stoian, S. A.; Bominaar, E. L.; Achim, C.; Dunbar, K. R. Properties of Prussian Blue Materials Manifested in Molecular Complexes: Observation of Cyanide Linkage Isomerism and Spin-Crossover Behavior in Pentanuclear Cyanide Clusters. *J. Am. Chem. Soc.* **2007**, *129*, 6104−6116.
(20) Rogez, G.; Parsons, S.; Paulsen, C.; Villar, V.; Mallah, T. A Prussian Blue Nanomolecule: Crystal Structure and Low-Temperature Magnetism. *Inorg. Chem.* **2001**, *40*, 3836−3837.
(21) Berseth, P. A.; Sokol, J. J.; Shores, M. P.; Heinrich, J. L.; Long, J. R. High-Nuclearity Metal-Cyanide Clusters: Assembly of a $Cr_8Ni_6(CN)_{24}$ Cage with a Face-Centered Cubic Geometry. *J. Am. Chem. Soc.* **2000**, *122*, 9655−9662.
(22) Schelter, E. J.; Karadas, F.; Avendano, C.; Prosvirin, A. V.; Wernsdorfer, W.; Dunbar, K. R. A Family of Mixed-Metal Cyanide Cubes with Alternating Octahedral and Tetrahedral Corners Exhibiting a Variety of Magnetic Behaviors Including Single Molecule Magnetism. *J. Am. Chem. Soc.* **2007**, *129*, 8139−8149.
(23) Groom, C. R.; Bruno, I. J.; Lightfoot, M. P.; Ward, S. C. The Cambridge Structural Database. *Acta Crystallogr., Sect. B:Struct. Sci., Cryst. Eng. Mater.* **2016**, *72*, 171−179.
(24) Clemente-León, M.; Coronado, E.; Martí-Gastaldo, C.; Romero, F. M. Multifunctionality in Hybrid Magnetic Materials Based on Bimetallic Oxalate Complexes. *Chem. Soc. Rev.* **2011**, *40*, 473−497.
(25) Thorarinsdottir, A. E.; Harris, T. D. Metal−Organic Framework Magnets. *Chem. Rev.* **2020**, *120*, 8716−8789.
(26) Coronado, E.; Galan-Mascaros, J. R.; Gomez-Garcia, C. J.; Laukhin, V. Coexistence of Ferromagnetism and Metallic Conductivity in a Molecule-Based Layered Compound. *Nature* **2000**, *408*, 447−449.
(27) Kitaev, A. Anyons in an Exactly Solved Model and Beyond. *Ann. Phys.* **2006**, *321*, 2−111.
(28) Nayak, C.; Simon, S. H.; Stern, A.; Freedman, M.; Das Sarma, S. Non-Abelian Anyons and Topological Quantum Computation. *Rev. Mod. Phys.* **2008**, *80*, 1083−1159.
(29) Gavriluta, A.; Claiser, N.; Kuhn, P.-S.; Novitchi, G.; Tommasino, J. B.; Iasco, O.; Druta, V.; Arion, V. B.; Luneau, D. Osmium-Nitrosyl Oxalato-Bridged Lanthanide-Centered Pentanuclear Complexes − Synthesis, Crystal Structures and Magnetic Properties. *Eur. J. Inorg. Chem.* **2015**, *2015*, 1616−1624.
(30) Kuhn, P.-S.; Cremer, L.; Gavriluta, A.; Jovanović, K. K.; Filipović, L.; Hummer, A. A.; Büchel, G. E.; Dojčinović, B. P.; Meier, S. M.; Rompel, A.; Radulović, S.; Tommasino, J. B.; Luneau, D.; Arion, V. B. Heteropentanuclear Oxalato-Bridged *nd*−4f (n = 4, 5) Metal Complexes with NO Ligand: Synthesis, Crystal Structures, Aqueous Stability and Antiproliferative Activity. *Chem. - Eur. J.* **2015**, *21*, 13703−13713.
(31) Zhang, X.; Cui, Y.; Zheng, F.; Huang, J. Synthesis and Structure of Novel Oxalate-Bridged Hexanuclear Lanthanide(III)-Chromium(III) Complexes. *Chem. Lett.* **1999**, *28*, 1111−1112.
(32) Mialane, P.; Dolbecq, A.; Costaz, G.; Lisnard, L.; Marrot, J.; Sécheresse, F. Synthesis and Structure of the First Dinuclear Lanthanide Oxalato Complexes $[\{Mo_2^{v}O_4(C_2O_4)_2(H_2O)_2\}_2\{(Ln_2(H_2O)_4)_2(C_2O_4)\}]\cdot 7H_2O$ (Ln = La^{3+}, Ce^{3+}). *Inorg. Chem. Commun.* **2002**, *5*, 702−705.
(33) Dean, P. A. W.; Craig, D. C.; Scudder, M. L.; Dance, I. G. The Crystallisation and Packing of $[Cr(C_2O_4Ag(PPh_3)_2)_3]$ $(Ph_3P/Ph_3PO)(MeNO_2)_4$. *CrystEngComm* **2008**, *10*, 1044−1046.
(34) Guo, S.; Zhan, W.-W.; Yang, F.-L.; Zhou, J.; Duan, Y.-H.; Zhang, D.; Yang, Y. Enantiopure Trigonal Bipyramidal Coordination Cages Templated by in Situ Self-Organized D_{2h}-Symmetric Anions. *Nat. Commun.* **2024**, *15*, No. 5628.

https://doi.org/10.1021/acs.cgd.5c00236
Cryst. Growth Des. 2025, 25, 5834−5844

(35) Martínez-Lillo, J.; Armentano, D.; De Munno, G.; Wernsdorfer, W.; Julve, M.; Lloret, F.; Faus, J. A Heterotetranuclear [$Ni^{II}Re_3^{IV}$] Single-Molecule Magnet. *J. Am. Chem. Soc.* **2006**, *128*, 14218−14219.
(36) Martinez-Lillo, J.; Armentano, D.; De Munno, G.; Wernsdorfer, W.; Clemente-Juan, J. M.; Krzystek, J.; Lloret, F.; Julve, M.; Faus, J. Heterotetranuclear Oxalato-Bridged ($Re_3^{IV}M^{II}$) (M = Mn, Fe, Co, Ni, Cu) Complexes: A New Example of a Single-Molecule Magnet (M = Ni). *Inorg. Chem.* **2009**, *48*, 3027−3038.
(37) Armentano, D.; Martínez-Lillo, J. Anion-Assisted Crystallization of a Novel Type of Rhenium(IV)-Based Salt. *Cryst. Growth Des.* **2016**, *16*, 1812−1816.
(38) Pei, Y.; Journaux, Y.; Kahn, O. Ferromagnetic Interactions between t_{2g}^3 and e_g^2 magnetic orbitals in a $Cr(III)Ni(II)_3$ Tetranuclear Compound. *Inorg. Chem.* **1989**, *28*, 100−103.
(39) *CrysAlis*. Oxford Diffraction Ltd.: Abingdon, England, 2006.
(40) *SCALE3 ABSPACK - An Oxford Diffraction Program (1.0.4,GUI:1.0.3)*; Oxford Diffraction Ltd.: Abingdon, England, 2005.
(41) Sheldrick, G. M. Crystal Structure Refinement with SHELXL. *Acta Crystallogr., Sect. C:Struct. Chem.* **2015**, *71*, 3−8.
(42) Dolomanov, O. V.; Bourhis, L. J.; Gildea, R. J.; Howard, J. A. K.; Puschmann, H. Olex2: A Complete Structure Solution, Refinement and Analysis Program. *J. Appl. Crystallogr.* **2009**, *42*, 339−341.
(43) Spackman, M. A.; Jayatilaka, D. Hirshfeld Surface Analysis. *CrystEngComm* **2009**, *11*, 19−32.
(44) Bain, G. A.; Berry, J. F. Diamagnetic Corrections and Pascal's Constants. *J. Chem. Educ.* **2008**, *85*, 532−536.
(45) Chilton, N. F.; Anderson, R. P.; Turner, L. D.; Soncini, A.; Murray, K. S. PHI: A Powerful New Program for the Analysis of Anisotropic Monomeric and Exchange-Coupled Polynuclear *d*- and *f*-Block Complexes. *J. Comput. Chem.* **2013**, *34*, 1164−1175.
(46) Kresse, G.; Joubert, D. From Ultrasoft Pseudopotentials to the Projector Augmented-Wave Method. *Phys. Rev. B* **1999**, *59*, 1758−1775.
(47) Blöchl, P. E. Projector Augmented-Wave Method. *Phys. Rev. B* **1994**, *50*, 17953−17979.
(48) Perdew, J. P.; Burke, K.; Ernzerhof, M. Generalized Gradient Approximation Made Simple. *Phys. Rev. Lett.* **1996**, *77*, 3865−3868.
(49) Krukau, A. V.; Vydrov, O. A.; Izmaylov, A. F.; Scuseria, G. E. Influence of the Exchange Screening Parameter on the Performance of Screened Hybrid Functionals. *J. Chem. Phys.* **2006**, *125*, No. 224106.
(50) Dudarev, S. L.; Botton, G. A.; Savrasov, S. Y.; Humphreys, C. J.; Sutton, A. P. Electron-Energy-Loss Spectra and the Structural Stability of Nickel Oxide: An LSDA+U Study. *Phys. Rev. B* **1998**, *57*, 1505−1509.
(51) Smyth, R. D.; Blandy, J. N.; Yu, Z.; Liu, S.; Topping, C. V.; Cassidy, S. J.; Smura, C. F.; Woodruff, D. N.; Manuel, P.; Bull, C. L.; Funnell, N. P.; Ridley, C. J.; McGrady, J. E.; Clarke, S. J. High- Versus Low-Spin Ni^{2+} in Elongated Octahedral Environments: $Sr_2NiO_2Cu_2Se_2$, $Sr_2NiO_2Cu_2S_2$, and $Sr_2NiO_2Cu_2(Se_{1-x}S_x)_2$. *Chem. Mater.* **2022**, *34*, 9503−9516.
(52) Ruiz Preciado, M. A.; Kassiba, A.; Morales-Acevedo, A.; Makowska-Janusik, M. Vibrational and Electronic Peculiarities of $NiTiO_3$ Nanostructures Inferred from First Principle Calculations. *RSC Adv.* **2015**, *5*, 17396−17404.
(53) Albavera-Mata, A.; Liu, S.; Cheng, H.-P.; Hennig, R. G.; Trickey, S. B. Magnetic and Thermodynamic Computations for Supramolecular Assemblies between a Cr(III) and Fe(III) Single-Ion Magnet and an Fe(II) Spin-Crossover Complex. *J. Phys. Chem. A* **2024**, *128*, 10929−10935.
(54) Neese, F.; Wennmohs, F.; Becker, U.; Riplinger, C. The ORCA Quantum Chemistry Program Package. *J. Chem. Phys.* **2020**, *152*, No. 224108.
(55) Weigend, F. Hartree−Fock Exchange Fitting Basis Sets for H to Rn. *J. Comput. Chem.* **2008**, *29*, 167−175.
(56) Weigend, F.; Ahlrichs, R. Balanced Basis Sets of Split Valence, Triple Zeta Valence and Quadruple Zeta Valence Quality for H to Rn: Design and Assessment of Accuracy. *Phys. Chem. Chem. Phys.* **2005**, *7*, 3297−3305.
(57) Baerends, E. J.; Ellis, D. E.; Ros, P. Self-Consistent Molecular Hartree-Fock-Slater Calculations I. The Computational Procedure. *Chem. Phys.* **1973**, *2*, 41−51.
(58) Dunlap, B. I.; Connolly, J. W. D.; Sabin, J. R. On Some Approximations in Applications of Xα Theory. *J. Chem. Phys.* **1979**, *71*, 3396−3402.
(59) Whitten, J. L. Coulombic Potential Energy Integrals and Approximations. *J. Chem. Phys.* **1973**, *58*, 4496−4501.
(60) Angeli, C.; Cimiraglia, R.; Evangelisti, S.; Leininger, T.; Malrieu, J. P. Introduction of *n*-Electron Valence States for Multireference Perturbation Theory. *J. Chem. Phys.* **2001**, *114*, 10252−10264.
(61) Angeli, C.; Cimiraglia, R.; Malrieu, J.-P. *N*-Electron Valence State Perturbation Theory: A Fast Implementation of the Strongly Contracted Variant. *Chem. Phys. Lett.* **2001**, *350*, 297−305.
(62) Angeli, C.; Cimiraglia, R.; Malrieu, J.-P. *n*-Electron Valence State Perturbation Theory: A Spinless Formulation and an Efficient Implementation of the Strongly Contracted and of the Partially Contracted Variants. *J. Chem. Phys.* **2002**, *117*, 9138−9153.
(63) Schapiro, I.; Sivalingam, K.; Neese, F. Assessment of n-Electron Valence State Perturbation Theory for Vertical Excitation Energies. *J. Chem. Theory Comput.* **2013**, *9*, 3567−3580.
(64) Heß, B. A.; Marian, C. M.; Wahlgren, U.; Gropen, O. A Mean-Field Spin-Orbit Method Applicable to Correlated Wavefunctions. *Chem. Phys. Lett.* **1996**, *251*, 365−371.
(65) Malmqvist, P.-Å.; Roos, B. O. The CASSCF State Interaction Method. *Chem. Phys. Lett.* **1989**, *155*, 189−194.
(66) Malmqvist, P.-Å.; Roos, B. O.; Schimmelpfennig, B. The Restricted Active Space (RAS) State Interaction Approach with Spin−Orbit Coupling. *Chem. Phys. Lett.* **2002**, *357*, 230−240.
(67) Chibotaru, L. F.; Ungur, L. Ab Initio Calculation of Anisotropic Magnetic Properties of Complexes. I. Unique Definition of Pseudospin Hamiltonians and Their Derivation. *J. Chem. Phys.* **2012**, *137*, No. 064112.
(68) Ungur, L.; Chibotaru, L. F. Ab Initio Crystal Field for Lanthanides. *Chem. - Eur. J.* **2017**, *23*, 3708−3718.
(69) Stoll, S.; Schweiger, A. EasySpin, a Comprehensive Software Package for Spectral Simulation and Analysis in EPR. *J. Magn. Reson.* **2006**, *178*, 42−55.
(70) Bénard, S.; Yu, P.; Audière, J. P.; Rivière, E.; Clément, R.; Guilhem, J.; Tchertanov, L.; Nakatani, K. Structure and NLO Properties of Layered Bimetallic Oxalato-Bridged Ferromagnetic Networks Containing Stilbazolium-Shaped Chromophores. *J. Am. Chem. Soc.* **2000**, *122*, 9444−9454.
(71) Coronado, E.; Martí-Gastaldo, C.; Galán-Mascarós, J. R.; Cavallini, M. Polymetallic Oxalate-Based 2D Magnets: Soluble Molecular Precursors for the Nanostructuration of Magnetic Oxides. *J. Am. Chem. Soc.* **2010**, *132*, 5456−5468.
(72) Hirshfeld, F. L. Bonded-Atom Fragments for Describing Molecular Charge Densities. *Theor. Chim. Acta* **1977**, *44*, 129−138.
(73) Mitsumi, M.; Okawa, H.; Sakiyama, H.; Ohba, M.; Matsumoto, N.; Kurisaki, T.; Wakita, H. The Dithiooxalate-Bridged Complex $[Cr(C_2O_2S_2)_3(NiL)_3][ClO_4]_3$(L = Racemic 5,5,7,12,12,14-Hexamethyl-1,4,8,11-Tetraazacyclotetradecane): Synthesis, Crystal Structure and Magnetism. *J. Chem. Soc., Dalton Trans.* **1993**, 2991−2994.
(74) Rebilly, J.-N.; Catala, L.; Rivière, E.; Guillot, R.; Wernsdorfer, W.; Mallah, T. A Tetranuclear $Cr^{III}Ni_3^{II}$ Cyano-Bridged Complex Based on M(Tacn) Derivative Building Blocks. *Inorg. Chem.* **2005**, *44*, 8194−8196.
(75) Liu, M.-J.; Hu, K.-Q.; Liu, C.-M.; Cui, A.-L.; Kou, H.-Z. Metallocyclic $Ni_4Ln_2M_2$ Single-Molecule Magnets. *Dalton Trans.* **2017**, *46*, 6544−6552.
(76) Hill, S.; Datta, S.; Liu, J.; Inglis, R.; Milios, C. J.; Feng, P. L.; Henderson, J. J.; del Barco, E.; Brechin, E. K.; Hendrickson, D. N. Magnetic Quantum Tunneling: Insights from Simple Molecule-Based Magnets. *Dalton Trans.* **2010**, *39*, 4693−4707.
(77) Atanasov, M.; Ganyushin, D.; Sivalingam, K.; Neese, F.A Modern First-Principles View on Ligand Field Theory through the Eyes of Correlated Multireference Wavefunctions. In *Molecular*

https://doi.org/10.1021/acs.cgd.5c00236
Cryst. Growth Des. 2025, 25, 5834−5844

Electronic Structures of Transition Metal Complexes II 2012; Vol. *143*, pp 149−220 .
(78) Lang, L.; Atanasov, M.; Neese, F. Improvement of Ab Initio Ligand Field Theory by Means of Multistate Perturbation Theory. *J. Phys. Chem. A* **2020**, *124*, 1025−1037.
(79) Doetschman, D. C. Electron Paramagnetic Resonance Studies of Transitionmetal Oxalates and Their Photochemistry in Single Crystals. I. $K_3[Cr(C_2O_4)_3]\cdot 3H_2O$ in $K_3[Al(C_2O_4)_3]\cdot 3H_2O$. *J. Chem. Phys.* **1974**, *60*, 2647−2653.
(80) Park, K.; Novotny, M. A.; Dalal, N. S.; Hill, S.; Rikvold, P. A. Effects of *D*-Strain, *g*-Strain, and Dipolar Interactions on EPR Linewidths of the Molecular Magnets Fe_8 and Mn_{12}. *Phys. Rev. B* **2001**, *65*, No. 014426.

https://doi.org/10.1021/acs.cgd.5c00236
Cryst. Growth Des. 2025, 25, 5834−5844